An Automated 2-D Line-Shift Measurement From Smoothed and Leveled Diagnostic Interferometric Images of Exploded-Wire Plasma

Michael A. Saville, *Senior Member, IEEE*, Andrew J. Hamilton, *Senior Member, IEEE*, and James E. Caplinger

***Abstract*— A novel, automated, 2-D line-shift measurement algorithm is presented for optical interferometry in plasma diagnostics. By using the smoothing and leveling (SL) algorithm as a preprocessing stage to the Fourier transform method (FTM), the proposed SL-FTM algorithm extracts the line shift without a priori knowledge of the spectral properties of the image, a common requirement of other FTM-based algorithms. The algorithm is simple to implement, and demonstrated for side-on views of plasma from exploded wires, where the interference patterns suffer from low contrast, low signal-to-noise ratio (SNR), and spatially varying intensity. SL-FTM and FTM are compared via Monte Carlo simulation of noisy images with realistic background variation. They are shown to have the accuracies of 0.019 and 0.016 lines, respectively. In addition, the cause of the accuracy difference is studied using a modified Jaccard similarity measure. The measure shows how SL-FTM provides a smoother phase surface than FTM, but underestimates the maximum line shift by up to 15%. Also, the well-known contour tracing method (CTM) is automated as SL-CTM. The automated forms of FTM and CTM (i.e., SL-FTM and SL-CTM) permit, for the first time, their direct comparison for a wide range of noisy images. SL-CTM, and by extension, CTM, achieves the best accuracy of 0.013 lines. Finally, each method is shown to have accuracy that exceeds the standard diagnostic accuracy requirement of 0.05 lines.**

***Index Terms*— Contour tracing method (CTM), Fourier transform method (FTM), interferometry analysis, smoothing and leveling (SL) algorithm.**

I. Introduction

OPTICAL interferometry is a powerful diagnostic tool for high density plasmas, where the plasma frequency is near the optical regime. It is noninvasive, accurate, with high temporal and spatial resolution, and is grounded in the straightforward physical connection between number density and refractive index. The 2-D relative phase shift is directly related to the line-integrated electron and neutral atomic densities as follows:

$$\Delta\phi(y,z) = \frac{2\pi\alpha}{\lambda}\int n_a \, \mathrm{d}x - 4.49\times 10^{-14}\lambda \int n_e \, \mathrm{d}x \quad (1)$$

where n_a represents the atomic density, n_e represents the electron density, α is the atomic polarizability, and $\Delta\phi$ is the relative interference phase shift. The constant in the second term implies units of cm for wavelength, cm^3 for polarizability, and cm^{-3} for densities [1]. Often, the phase shift from neutrals is assumed negligible in the above equation, and the total electron content can be readily measured. Though for the experimental conditions examined in this work, and similar partially ionized wire explosions, direct determinations of electron density cannot be made without a priori knowledge of neutral density, as neither term in (1) is dominant. To measure both densities, two interferograms are obtained simultaneously at two wavelengths (e.g., 532 and 1064 nm), and (1) is duplicated for each wavelength leaving two equations and two solvable unknowns, the line-integrated atomic and electron densities [2], [3]. However, the utility of this diagnostic tool is hindered by the common necessity and associated error of manual fringe to phase reckoning and the lack of algorithms suitable for automation.

The Fourier transform method (FTM) for phase analysis of interferograms is well known for its versatility to extract the 2-D phase function in a wide variety of applications [4], [5], [6]. As the fringe lines present a 2-D spatial frequency that is modulated with the desired phase function, FTM is similar to a heterodyne process. It demodulates the image from the 2-D spatial frequency (represented by the reference fringe lines) and then filters the baseband content centered at zero frequency (dc) to recover the relative phase change caused by the plasma. However, in order to recover the spectral response from the dc background, FTM requires careful selection of the spatial-carrier filter [7]. Furthermore, FTM relies on well-defined fringe lines.

Recently, two iterative methods have been developed to improve the 2-D phase recovery. The straightforward approach in [8] evaluates the 2-D phase spectra of the dc term and the bandwidth of the spatial carrier. However, the requisite number of iterations is highly dependent on the data, and the method suffers when the image has low contrast that occurs in

Manuscript received 30 June 2022; revised 13 December 2022 and 4 February 2023; accepted 5 December 2023. Date of publication 3 January 2024; date of current version 12 January 2024. This work was supported by the Air Force Office of Scientific Research through the Sensors Directorate, U.S. Air Force Research Laboratory, under Award LRIR 16RYC0R289. The views expressed in this article are those of the authors and do not reflect the official policy or position of the U.S. Air Force, Department of Defense, or the U.S. Government. The review of this article was arranged by Senior Editor S. Portillo. *(Corresponding author: Michael A. Saville.)*

Michael A. Saville is with the Department of Electrical and Computer Engineering, Air Force Institute of Technology, Wright-Patterson AFB, Dayton, OH 45435 USA (e-mail: michael.saville@ieee.org).

Andrew J. Hamilton and James E. Caplinger are with the U.S. Air Force Research Laboratory, Wright-Patterson Air Force Base (AFB), Dayton, OH 45433 USA.

Color versions of one or more figures in this article are available at https://doi.org/10.1109/TPS.2023.3341258.

Digital Object Identifier 10.1109/TPS.2023.3341258

z-pinch plasma diagnostics [9], [10], [11]. The model-fitting iterative approach of [12] increases FTM accuracy by an order of magnitude. However, its least squares fitting of a 36-order Zernike polynomial is complicated and requires additional 2-D interpolation to transform from Cartesian to Polar coordinates. Also, the accuracy is degraded in cases of weak contrast and spatially varying brightness in which Nakayama et al. [12] rely on additional iterative algorithms.

The typical four-step approach to reconstruct the relative phase from z-pinch and exploded-wire plasma interferometry is what we refer to as the contour tracing method (CTM). The steps are as follows: 1) measure the fringe line shifts of the test and reference images by manually tracing the fringe lines (or the nulls as in [9]); 2) assign integer multiples of 2π to the traced lines representing level contours of a surface; 3) interpolate the set of lines (contours) to a surface representing the unwrapped relative phase; and 4) calculate the relative phase difference between the reference and test phases resulting from steps 1) to 3). As described in [9] and [10], the line shift measurement is based on a tedious visual inspection of the image and requires use of specialized photograph and image enhancement software to increase the clarity of the lines. Also, according to [9], the phase assignment of step 2) is aided by an unspecified algorithm, which is presumably a mental model of how the analyst interprets the spatial relationship between neighboring lines. In this work, we employ such an algorithm for single-wire interference patterns. The surface interpolation returns a smooth phase profile and represents the best possible phase reconstruction from the noisy image. For comparison of the two approaches, CTM is considered the standard.

Here, the smoothing and leveling (SL) algorithm first proposed in [11] for 1-D phase reconstruction from side-on views of single exploded-wire interferometry is modified for 2-D fringe shift measurement. The SL algorithm is combined with CTM as SL-CTM and with FTM as SL-FTM. Each algorithm automatically extracts the fringe shift from monochromatic interferograms. The SL stage reduces the fringe amplitude variability to produce well-defined fringe lines, thus making them easier to automatically trace for CTM. In context of FTM, the process effectively removes the dc background term and normalizes the fringe intensity throughout the image. Hence, it is easier to design the spatial carrier filter for FTM without a priori knowledge of the spectral properties of the image and without need of iterative filtering. In the case of diagnostic plasma interferometry, which has highly varying brightness and weak contrast [13], the proposed SL-FTM and SL-CTM algorithms are shown to reconstruct the relative phase with an accuracy of ± 0.06 radians (i.e., a shift error $<$ 0.02 lines), which exceeds the standard accuracy requirement (0.05 lines [14]) needed to recover volumetric atom and electron densities.

In the following, Section II reviews the phase recovery process with FTM followed by a description of SL-FTM and SL-CTM in Section III. Section IV presents an example with measured data and then assesses the accuracy using Monte Carlo simulation of known interference images with spatially varying intensity and additive noise. Also, the simulated backgrounds are adaptations of measured background profiles from single-wire diagnostics. The detailed presentation of SL-FTM shows how it is simple to implement without the need of iterative optimization. Finally, Section V presents discussion and conclusions about the underlying assumptions and application of SL-FTM and SL-CTM.

II. Reconstruction of the 2-D Phase Function

A. Interference Pattern Model

The interferometric images used in this work are captured in the small-scale wire explosion experiment of [11]. In summary, the electrical source for the explosion is a benchtop 80-kV, 2.5-kA pulse power supply with a 10-ns rise time. The power is coupled, in this case, to 25-μm-diameter aluminum wires in a small vacuum chamber between brass electrodes with $\approx$ 1-cm spacing. Wire explosion dynamics are captured primarily using refraction-based optical techniques, driven by a Q-switched Nd:YAG laser with a 10-ns pulsewidth, and frequency doubled, so that both the 1064-nm fundamental mode and the 532-nm second harmonic may be utilized.

The commonly used Mach–Zehnder-type interferometer was used for this work. It consisted of a collection of lenses, mirrors, and beamsplitters, which split the incident plane wave ($E = E_0 e^{-jkx}$) into a reference beam and a probing beam that travel through a common segment of ambient air and then through different paths of unequal optical lengths. The reference path is entirely in air, and the probing beam traverses air, two vacuum chamber windows, a vacuum (<10 mTorr), and the ionized material. The reference and probing beams are combined at a beamsplitting cube before the camera, focused, and after passing through wavelength and density filters irradiate the camera as follows:

$$E(y,z) = E_0 e^{-jk_0 L}\left[e^{-jk_0 \delta L} + e^{-jk_0 \int_\ell n \ \mathrm{d}x}\right]. \tag{2}$$

In (2), the reference frame is defined with x along the optical path, and the yz plane is in the camera's focal plane. Also, the initial electric field strength is E_0, and the plasma's index of refraction n is nonhomogeneous. The common path segment has length L, and δL is the path length differential imposed by the interferometer. However, the plasma has an irregular cross section, and the path through the plasma has a spatially varying length $\ell(y,z)$, which causes 2-D phase variation. Finally, the conventional uniform plane wave notation in (2) accommodates the lossy nature of the plasma region. When lossy, the index of refraction is complex, and the imaginary part has a sign consistent with an attenuating propagation.

The measured field intensity ($I \propto |E|^2$) at the camera includes nonideal radiometric effects caused by the beams, optical components, and the plasma. The intensity at pixel (y,z) is modeled as follows:

$$I(y,z) = a(y,z) + b(y,z)\cos\left[\kappa_y y + \kappa_z z + \phi(y,z)\right]. \tag{3}$$

In (3), a is the background contribution, b is the fringe intensity variation, and κ_y and κ_z are the spatial frequencies. The normalized pixels in the N-bit digital image have quantized values in $[0, 1-2^{-N}]$ and result in a strong dc component. However, the cumulative radiometric effects spread the spectra of a and b causing overlap and complicating reconstruction

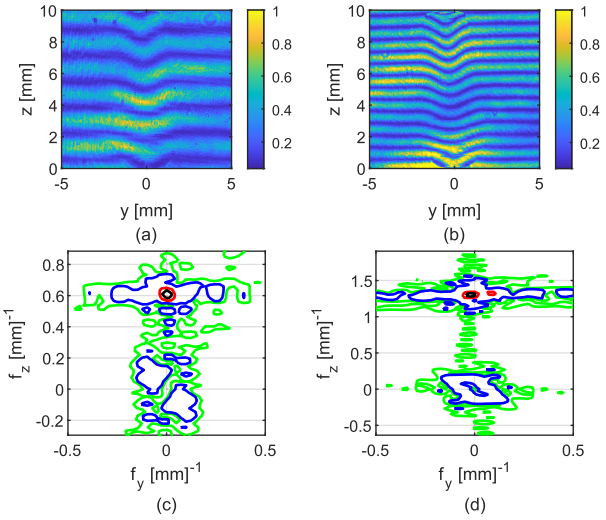

Fig. 1. Unprocessed images of Al plasma at 200 ns after wire explosion (a) 1064 and (b) 532 nm. (c) and (d) Contours of the Fourier power spectra in dB, respective of (a) and (b). The lines are powers in dB at −13 (green), −10 (blue), −3 (red), and −1 (black), relative to the peak at the spatial carrier.

of ϕ. Fig. 1(a) and (b) shows the interference images of the 1064- and 532-nm diagnostics of Al plasma at 200 ns after wire explosion. The fringe lines have varying brightness and low contrast but especially so in the 532-nm image.

Fig. 1(c) and (d) shows the contours of the 2-D energy spectra of Fig. 1(a) and (b). The black contour denotes the −1-dB level, and the levels at −3, −10, and −13 are represented by red, blue, and green contours, respectively. We also note how the background term a has been removed as $I - \langle I \rangle$, and before applying the discrete Fourier transform (DFT), where $\langle I \rangle$ is the mean intensity of the image. If the background is not removed, the dc energy term dominates. By removing the dc energy first, it is easier to observe how the spectra of the fringe line shift are generally separated from the dc term, but often poorly without prefiltering the images. In context of the FTM filter size, to be discussed in the next section, the −10-dB contour shows how the residual dc energy significantly influences the 2-D filter bandwidth, which is critical for accurate phase reconstruction.

B. FTM Algorithm

FTM is particularly useful for surface profilometry, because the interference patterns are based on reflection from an irregularly shaped but stable surface. The phase can be recovered from a single image when the images have strong contrast, and the fringe lines are generally clearly visible and reproducible. Even if a reference image is unavailable, the phase function can be recovered with high accuracy. However, for the z-pinch plasma diagnostic where the plasma volume develops differently with each experiment and with varying refractive index, the fringe lines have significant intensity variation. A reference image is often required to provide a phase reference unlike profilometry. In cases where the field of view is large enough to include the segments of the fringe lines that are unperturbed, a single image will suffice. Here, we assume that a reference image is taken before wire explosion, and the test image is taken soon afterward. The fringe lines of the reference image

Algorithm 1 FTM [6]

Input

I input grayscale image

Output

$\tilde{\phi}$ unwrapped phase

Start

1. Measure spatial frequencies κ_y and κ_z
2. Demodulate I to baseband and low-pass filter as

$$c(y,z) = h(y,z) * \left[I(y,z) e^{i\kappa_y y} e^{i\kappa_z z} \right],$$

3. Recover the wrapped phase ϕ as

$$\phi(y,z) = \arctan\left(\frac{\mathcal{I}m\{c(y,z)\}}{\mathcal{R}e\{c(y,z)\}} \right).$$

4. Unwrap phase: $\tilde{\phi} = \text{unwrap}(\phi)$

generally align well with the fringe lines of the test image. Therefore, we apply FTM to each image and calculate the relative phase difference as $\Delta\phi = \phi_{\text{test}} - \phi_{\text{ref}}$, where ϕ_{ref} and ϕ_{test} are the recovered reference and test phase profiles, respectively.

The conventional FTM algorithm consists of four steps listed in Algorithm 1 [6]. The first step to measure the spatial frequencies κ_y and κ_z can be accomplished with the 2-D DFT or by visual inspection of the fringe line spacings along y and z. We use a DFT process with a peak detection algorithm that identifies the energy peak away from dc and measures κ_y and κ_z. In the second step, the image is demodulated to baseband and filtered as follows:

$$c(y,z) = h(y,z) * \left[I(y,z) e^{j\kappa_y y} e^{j\kappa_z z} \right] \tag{4}$$

where h is an ideal 2-D rectangular window function with size $Q_y \times Q_z$, $Q_y = \lceil 2\pi/\kappa_y \rceil$, $Q_z = \lceil 2\pi/\kappa_z \rceil$, $\lceil \cdot \rceil$ is the ceiling operation, and $*$ denotes 2-D convolution. The third step is to calculate the phase as follows:

$$\phi(y,z) = \tan^{-1}\left(\frac{\mathcal{I}\text{m}\{c(y,z)\}}{\mathcal{R}\text{e}\{c(y,z)\}} \right). \tag{5}$$

The last step is to unwrap the phase. In our experience with single- and double-wire experiments, the phase unwrapping was trivial, but as we expect complex interference patterns, such as from the end-on view of multiwire z-pinch experiments, it may be necessary to employ advanced phase unwrapping techniques, such as phase gradients [15] or graph cuts [16].

The main FTM principles of [6], [12], and [8] are to demodulate the image to the baseband spatial frequencies, where the spectrum of $c = be^{j\phi}$ is centered at dc. When the fringe lines are densely spaced, or have a relatively high spatial frequency, the spectral content of c is nicely separated from the spectrum of a as in Fig. 1(d). However, the phase reconstruction degrades when there is significant spectral overlap of the dc and carrier regions as in Fig. 1(c).

Fig. 2 shows the measured background intensity a and fringe intensity variation ($b = \sqrt{c^* c}$) of the images in Fig. 1. In the 1064-nm spectrum, the background a has sufficient

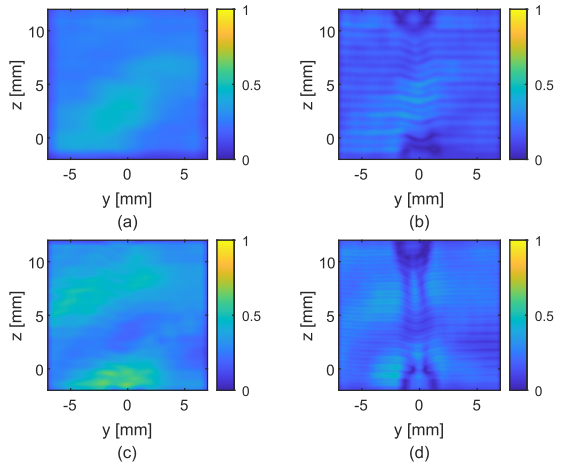

Fig. 2. Background intensity a from (a) 1064- and (c) 532-nm images of Fig. 1, respectively, and (b) and (d) corresponding fringe intensity variation b.

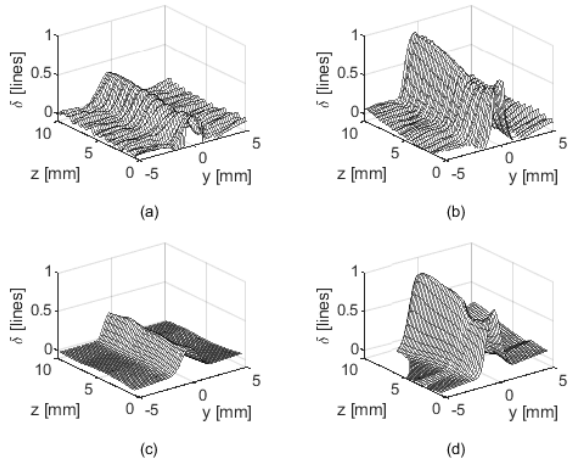

Fig. 3. Phase shift in units of lines reconstructed from Fig. 1(a) and (c). (a) FTM at 1064 nm. (b) FTM at 532 nm. (c) CTM at 1064 nm. (d) CTM at 532 nm.

bandwidth that even after filtering, c and b show rippling. The background function a and fringe intensity b represent the varying brightness and weak contrast that cause distorted phase profiles from FTM. Fig. 3 shows the recovered phase functions after conversion to normalized line shift [$\delta = \Delta\phi/(2\pi)$] for FTM and CTM. It is notable here that in Fig. 3, the phase shift at 532 nm is nearly twice that of the 1064-nm phase shift, indicating a dominance of the neutral term in (1), for this particular time in the detonation. Line units are convenient for measuring accuracy and for comparing results of FTM with CTM, because the height of the surface δ is the line shift observed in the interferogram. The overlapped spectra of a and c appear in Fig. 3(a) and (b) as rippling, which degrades the 2-D density measurement in the plasma diagnostic.

III. Smoothed and Leveled FTM and CTM

A. SL Algorithm

When the images are noisy or have very low contrast, it is difficult to visually calculate the fringe shift. The SL algorithm sharpens the fringe lines using a three-stage approach: 2-D Gaussian blurring, 1-D low-pass filtering (smoothing), and 1-D amplitude leveling. Although the algorithm was introduced in [11] as a preprocessing step for a 1-D fringe-ratio extraction algorithm, the mathematical description and parameters were undefined. In the following, the details are provided, and the algorithm is improved for 2-D to show how SL makes SL-FTM much easier to implement than the recently reported iterative methods of [8] and [12].

Algorithm 2 SL Algorithm

Input
I unprocessed image of size $M \times N$
Output
$\tilde{I}$ smoothed and leveled image of size $M \times N$

Step 1 Apply 2D Gaussian smoothing filter ▷ *optional*

Start *smoothing and leveling*

Step 2 Smooth s_m
for each vector $s_m = I(y_m, z)$ **do**
Filter s_m as $\tilde{s}_m = h_m * s_m$ using (9)
end for

Step 3 Level $\tilde{s}_m$
for each vector $\tilde{s}_m = I(y_m, z)$ **do**
Form non-overlapping segments of z
a. Find extrema of $\tilde{s}_m(z) : \{z_c, \tilde{s}_m(z_c)\}$
b. Partition z into J intervals
$\tilde{z} = \{\min(z), z_c, \max(z)\}$

for For each interval $\tilde{z}_j$ **do**
Scale $\tilde{s}_m(z)$ to the peak magnitude $A = 1$ as
if $\tilde{s}_m(z_c) \geq 0$ **then**
$\tilde{s}_m(z) = +\frac{A}{\max \tilde{s}_m(z)} \tilde{s}_m(z), \quad z \in \tilde{z}_j$
else if $\tilde{s}_m(z_c) < 0$ **then**
$\tilde{s}_m(z) = -\frac{A}{\min \tilde{s}_m(z)} \tilde{s}_m(z), \quad z \in \tilde{z}_j$
end if
end for
end for

The SL algorithm is listed in Algorithm 2. In the first step, a 2-D Gaussian kernel is applied to the unprocessed image as follows:

$$\tilde{I}(y, z) = \left(\frac{1}{2\pi\sigma^2} e^{-\frac{y^2+z^2}{2\sigma^2}} \right) * I(y, z) \tag{6}$$

where σ is experimentally determined to be 0.1–0.2 W for a digital filter width W. The filter width is determined by visual inspection of the high-frequency ripple along the fringe lines. In an automated approach, a 2-D spectral analysis can identify the high frequencies and determine the filter width. In cases where images have low noise or negligible high-frequency noise, this step is skipped.

The smoothing stage assumes linear fringes and accommodates lines with tilt as seen in [11]. For horizontal fringe lines and an image of size $N \times M$, each column of the image is modeled as a discrete sinusoidal signal plus additive white

Gaussian noise as follows:

$$s_m[n] = I[n, m] = I(y_m, z_n) \tag{7}$$

$$= a_0 + a_m \cos(\kappa_z z_n + \phi_0) + \eta[n] \tag{8}$$

where $m = 1, \ldots, M$, $n = 1, \ldots, N$, a_0 is the dc bias, a_m is the signal amplitude, and η is the noise. A biased second-order difference filter is applied as $h_m * s_m + b_m$ where the filter is augmented with sliding-average filters as follows:

$$h_m = K_m[h_w * (h_d * \{h_w * [h_d * (h_w * \delta)]\})] \tag{9}$$

and

$$h_w[n] = \text{rect}\left(\frac{n}{W}\right), \qquad n = 1, \ldots, W \tag{10}$$

$$h_d[n] = (-1)^{n-1}, \qquad n = 1, 2 \tag{11}$$

$$K_m = \frac{\text{range}(h_w * s_m)}{\text{range}(h_w * h_d * h_w * h_d * h_w * s_m)} \tag{12}$$

$$b_m = \text{median}(s_m). \tag{13}$$

In (12), the range$(\cdot)$ operation returns the peak-to-peak value. Although a single sliding-average filter can be used for h_m, it tends to blur the low-contrast regions beyond recovery. The cascaded first-order filters with intermediate sliding-average filters take advantage of the large discontinuities caused by numerical derivatives, and they actually preserve the amplitude variation of the fringe patterns. The bias b_m ensures that the median level of s_m is retained if needed. However, it is generally omitted in the amplitude leveling step. Thus, the smoothing step effectively removes $a(y, z)$ from (3).

The amplitude leveling stage finds the critical points of each sinusoid and scales the peak-to-peak values to $[-1,1]$. The complete SL algorithm is listed in Algorithm 2. After the smoothing stage and the initial check for critical points, there are residual localized extrema that are excluded through a check of $|s_m(z_c)| \leq 0.1 \max(|s_m(z)|)$. The remaining extrema tend to be clustered about the positive and negative peaks of the sinusoid. Thus, the final set of z_c is selected as the maxima ($s_m \geq 0$) and minima ($s_m < 0$) and is used to partition z into J intervals. The scaling step is straightforward, and with $A = 1$, it effectively normalizes $b(y, z)$ in (3). The resulting smoothed and leveled image $\tilde{I}(y, z) \approx \cos(\kappa_y y + \kappa_z z + \phi(y, z))$.

We note a limitation of the leveling algorithm. As described in (8) and in Step 3 of Algorithm 1, each filtered signal $\tilde{s}_m$ is partitioned into multiple segments according to the critical points. Each partition is rescaled to ± 1, but in some cases where the signal-to-noise ratio (SNR) is very low (<3 dB), the rescaling can fail. As an example, in Fig. 1(b), near $y = 4.5$ mm and $z = 2.25$ mm, the SNR is less than < 3 dB. The corresponding region in Fig. 4(b) has segments of the fringe line that are improperly scaled resulting in faint segments along the fringe line. However, as FTM is a spectral domain algorithm, the small number of faint pixels has negligible effect. Also, the automated CTM (SL-CTM), and its use of curve fitting, inherently overcomes breaks in fringe lines.

B. SL-FTM

SL is a prefiltering step with FTM and is similar to other image processing methods used to improve the clarity of the fringe patterns [17]. SL-FTM is particularly useful for fringe curves that are open and linear. When closed loops occur in the interference pattern, the leveling algorithm would need to be modified. However, for the side-on view of the exploding wire experiments, the fringes are linear and open. Hence, the smoothed and leveled image is input to FTM and processed according to Algorithm 1.

We note how SL-FTM is applied to both the reference and test images, and the spatial carrier frequency can be measured from the reference image. However, we use the test image to measure κ_x and κ_y out of convenience, as we also need to measure the spatial bandwidth of the test image (part of the FTM algorithm), and to demonstrate the relative phase measurement when a reference image is unavailable. Hence, the reference image is only used to calculate $\Delta\phi$, as described in Section II-B. Also, when the fringe lines of the reference and test images are nicely aligned, $\min \Delta\phi = 0$ and $\Delta\phi > 0$. This condition is convenient for the Monte Carlo analysis where we measure the difference between the known phase surface and the recovered phase surface. When the reference image is unavailable, a minimum value correction is applied to ensure $\min \Delta\phi = 0$, as discussed in Section IV.

C. SL-CTM

In addition to direct 2-D analysis using FTM, we found the SL filter suitable for automated fringe line extraction as part of CTM. The leveling stage returns images with pixel amplitudes in $[-1, 1]$. In [11], fringe lines are extracted by treating the image as a surface and then finding the contours that correspond to positive peaks, which are the fringe lines. Each contour forms a closed loop around the pixels representing the fringe lines. Then, the 2-D coordinates of each contour are averaged to calculate the line segment along the middle of the contour. The resulting line segments are the fringe lines. When the image has very low SNR, a single fringe line may be represented by several contours, and the leveling algorithm may fail to properly scale some sections of the fringe lines as discussed in Section III-A.

In those cases, multiple line segments will represent the same fringe line. When we have only a few images to analyze, we manually associate the segments to a single fringe line. The process takes only a few seconds for each image, but it becomes highly impractical when there are many images to analyze and motivates the development of an automatic line fitting step. The last step of SL-CTM is to fit the line segments to their fringe line with an appropriate curve. For the single-wire interferograms, we use a straight line to fit the fringe lines in the reference image and a Gaussian curve to fit the test-image fringes. However, when the fringe lines have tilt, i.e., they are not purely horizontal or purely vertical, we also ensure that the Gaussian model includes the same tilt as the reference lines. When the reference image is unavailable, the regions of the test image where the fringe lines are straight can be used to determine tilt correction.

Therefore, with appropriate programming, we automate the line tracing step of SL-CTM to save considerable time. The details of how we implement SL-CTM are not shown here, because the purpose of SL-CTM is to serve as a reference

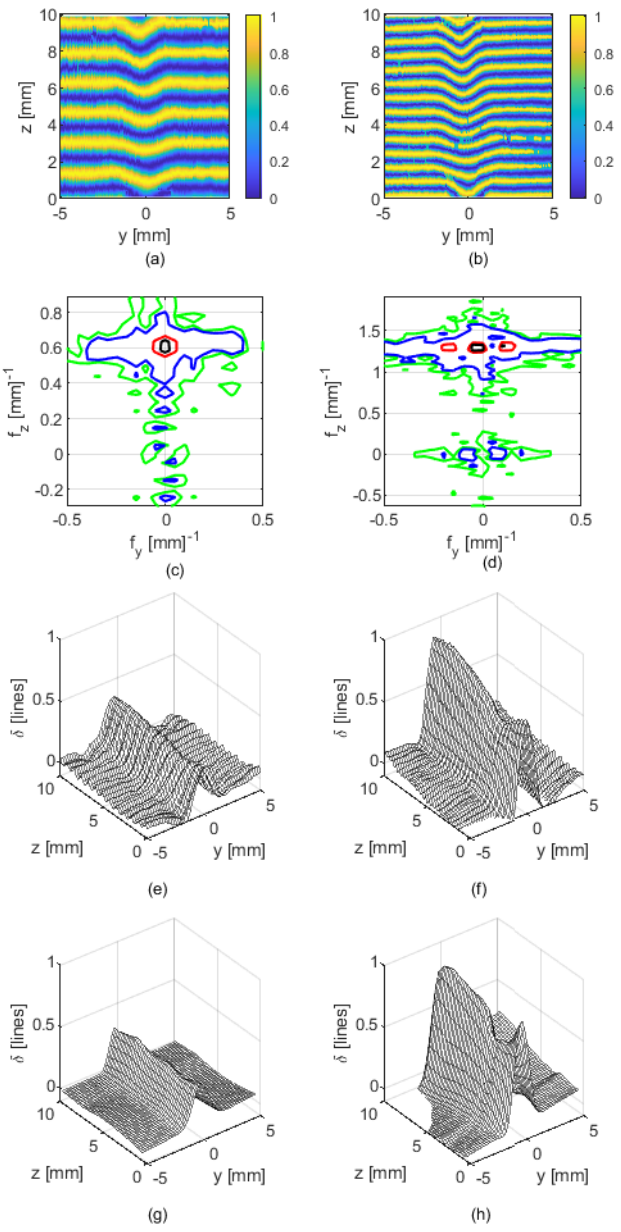

Fig. 4. (a) and (b) Smoothed and leveled interferometric images of Al plasma at 200 ns after wire explosion corresponding to Fig. 1(a) and (b). (c) and (d) 2-D contours of the respective energy spectra in dB (black: −1 dB, red: −3 dB, blue: −10 dB, and green: −13 dB). (e)–(h) 2-D relative phase in units of lines measured with (e) and (f) SL-FTM and (g) and (h) SL-CTM.

for the error analysis of SL-FTM, and the authors intend to report SL-CTM in a future publication. In Section IV, we demonstrate processing of over 500 2-D images with SL-FTM and SL-CTM in a Monte Carlo error analysis.

IV. Results

A. Examples of Measured Data

Fig. 4(a) and (b) shows how after SL filtering, the images of Fig. 1(a) and (b) have noticeably improved fringe lines improving the ease and accuracy of calculation. Also, the spectra of Fig. 4(c) and (d) show how the dc energy is significantly removed when compared with Fig. 1(c) and (d). Thus, it is straightforward to implement the algorithm to find and associate the strongest spectral energy with the spatial carrier. Also, the algorithm can easily find the spatial bandwidth of the fringe shift by finding where energy drops to a specified level relative to the peak (e.g., −10 dB). The algorithm when implemented in a computer program operates without any knowledge of the spatial carrier frequency or the bandwidth about the carrier, which is a distinct advantage of using SL as a preprocessing step for FTM. In addition, the filter removed the high frequency variation observed in the fringe lines as caused by the interferometer.

Fig. 4(e)–(h) shows the SL-FTM and SL-CTM reconstructed phase shift $\Delta\phi$. The normalized phase shift $\delta = (1/2\pi)(\Delta\phi(y,z) - \min \Delta\phi(y,z))$. Due to the relative measurement, the minimum value correction ensures that the 2-D line shift profile starts at zero. The minimum value is selected where δ is far from the peak, i.e., $|y| > 3.0$ mm.

For the 532-nm data, the relative phase surface is smoother with SL-FTM than FTM as expected, because the dc term is sufficiently isolated from the energy about the spatial carrier. However, there is still dc leakage in the 1064 nm, which appears as rippling along the surface. In general, SL-FTM provides smoother 2-D phase than FTM. However, SL-FTM, being a filtering operation, removes energy from the intensity spectrum and underestimates the height of phase surface much like well-known digital windowing functions. To compare the results of FTM and SL-FTM with the standard CTM, we perform a Monte Carlo analysis in the next section. However, we use SL-CTM as a surrogate for CTM, because it is impractical to manually trace the fringe lines in CTM for hundreds of noisy images. As SL-CTM is based on CTM with error sources resulting from the line fitting step, we consider SL-CTM as a worst case of CTM.

B. Error Analysis

The typical line shift error tolerance reported for density measurements [10], [14] is 0.05 lines and is based on the ability to resolve the line shift in a noisy image. According to [14], the line shift tolerance is equivalent to a density accuracy of 5%–7% for Gaussian fringe curves. However, it is important to note how the phase is related to the line integral of the density function, whereas the FTM literature assesses FTM error by simulating an interferogram of a stable surface that has a specified variance given as peak-to-valley ratio in units of wavelength. The accuracy of the profilometry measurement is directly proportional to the reconstructed phase. Thus, when the reconstructed phase is compared with the known phase and reported as root-mean-square error (RMSE) [12], [18], the error is a direct report of the profilometry accuracy.

To assess the effect of SL on FTM and CTM, we measure the difference between a known relative phase function $\phi(y,z)$ for $y \in [-3,3]$, $z \in [0,10]$ and the reconstructed phase from a noisy image with spatially varying effects. We simulate a set of interferograms as $a + b\cos(\kappa_y y + \kappa_z z + \phi + \phi_0) + \eta$, where ϕ_0 is a uniform random variable in $U[0,2\pi]$, $b = 0.5$, and η is a zero-mean Gaussian random variable with variance set for signal-plus-background-to-noise ratio (SBNR) $(a+b)/\eta$ in $[-10, 23]$ dB. The background a is randomly selected from a set of 14 previously measured backgrounds [13] and is

randomly rotated and scaled to increase the variability. The scale factor of a sets the signal-to-background ratio (SBR) $(a/b) \in [0.25, 2.5]$.

Each simulated interference image is processed using FTM, SL-FTM, and SL-CTM, and the resulting line shifts are compared with the known profile $\phi/(2\pi)$ as RMSE with units of lines. However, we note how the RMSE fails to show where or how the difference is significant. Therefore, we also compare the line shift surfaces (e.g., Fig. 4) using the Jaccard similarity measure with index $J = (|\mathcal{A} \cap \mathcal{B}|/|\mathcal{A} \cup \mathcal{B}|)$. The Jaccard index is the ratio of the size of the intersection of sets $\mathcal{A}$ and $\mathcal{B}$ to the size of their union. When the two sets are identical, $J = 1$, and when the sets are mutually exclusive, $J = 0$.

As the domains of the reference and noisy phase profiles are the same, we define $\mathcal{A}$ as the set of pixels, where $\Delta\delta = \delta_{\text{sim}} - \delta_{\text{ref}} < 0.05$. The subscripts sim and ref denote the reconstructed simulated and known reference line-shift profiles, respectively. Set $\mathcal{B}$ is defined as the pixels with $\nabla\delta_{\text{sim}} \cdot \nabla\delta_{\text{ref}}/|\nabla\delta_{\text{sim}}||\nabla\delta_{\text{ref}}| < 0.05$. Set $\mathcal{B}$ is the set of pixels where the surface gradients of the reconstructed phase profile have directions within $\pm 22.5°$ of the known phase profile. Thus, the Jaccard index gives insights into how the phase profiles differ better than the RMSE measure.

1) Varying Signal to Noise With Constant Background: First, we simulate 30 images for each level of additive noise and a fixed SBR of 0.5. As in a dual-wavelength measurement, a pair of reference (before wire explosion) and test images are simulated for each wavelength. At 1064 nm, the spatial carrier frequencies are $\kappa_z = 2\pi/1.8$ and $\kappa_y = 2\pi/500$ and are doubled for the 532-nm image. For computational efficiency, we limited the pixel sizes to 0.02 mm, and the frequencies were set to avoid image aliasing.

The reference image phase is zero-mean Gaussian as follows:

$$\phi_{\text{ref}}(y, z) \sim \mathcal{N}\left(0, \pi^2 \times 10^{-2}\right) \tag{14}$$

where $\mathcal{N}(\mu, \sigma^2)$ denotes the Gaussian distribution with mean μ and variance σ^2. The test image phase after wire explosion has the skewed Gaussian profile

$$\phi_{\text{test}}(y, z) = \pi \exp\left[-(z/10 + y - 0.1)^2 \pm \pi/60\right]. \tag{15}$$

In (15), the constant $\pm\pi/60$ is toggled randomly for each test image.

There are two important notes. First, we expect the SL filtering operation to lose some information in the original image. Therefore, we run FTM and SL-FTM with the same filter h. This approach allows us to observe if and how SL filtering might limit the accuracy. Second, the spatially varying background spreads the energy about the dc component and hinders the automated peak detection algorithm with FTM. Rather than use a sophisticated signal detection algorithm, we simply use SL-FTM first, which can easily identify the non-dc energy and return (κ_y, κ_z). Then, we run FTM with the same frequency and find h for the 10-dB spatial bandwidth about (κ_y, κ_z). Finally, we rerun SL-FTM with (κ_y, κ_z) and filter h. Hence, the Monte Carlo process is fully automated and is a significant advantage of using SL-FTM.

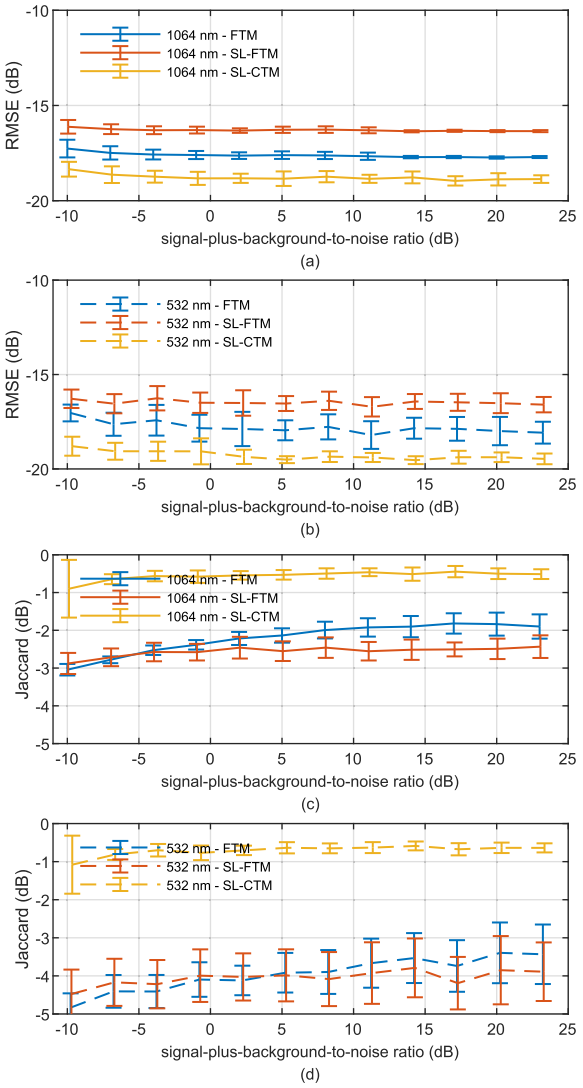

Fig. 5. Accuracy with varying SBNR and fixed SBR = 0.5. (a) 1064-nm RMSE. (b) 532-nm RMSE. (c) 1064-nm Jaccard index. (d) 532-nm Jaccard index.

The RMSE trends shown in Fig. 5(a) and (b) are the same for the 1064- and 532-nm simulations where SL-CTM achieves the smallest accuracy at −18 to −19 dB (equivalent to 0.013–0.016 lines). FTM and SL-FTM errors are −17.5 and −16.25 dB (or, 0.019 and 0.024 lines), respectively. The flat curves indicate the robustness of each method to the additive noise. However, the Jaccard indices shown in Fig. 5(c) and (d) offer greater insight into how much more the SL-CTM phase profile agrees with the known phase profile than the FTM-based solutions. Where the SL-CTM index ranges from −0.75 to −0.5 dB (0.8–0.9), FTM and SL-FTM only reach −1.75 dB (0.67) for 1064 nm and −3.4 (0.46) for 532 nm. Analysis of the sets $\mathcal{A}$ (local height difference) and $\mathcal{B}$ (local gradient difference) reveals how SL-FTM underestimates the height of the Gaussian phase surface and has fewer pixels that are less than 0.05 lines from the true surface. Also, both of the SL-FTM and FTM solutions have oscillatory behavior, and nearly half of the pixels have gradient directions greater than 22.5° from the true direction. In the case of the 532-nm images, the oscillations are twice those in the 1064-nm image and result in a much smaller set $\mathcal{B}$ than the 1064-nm set.

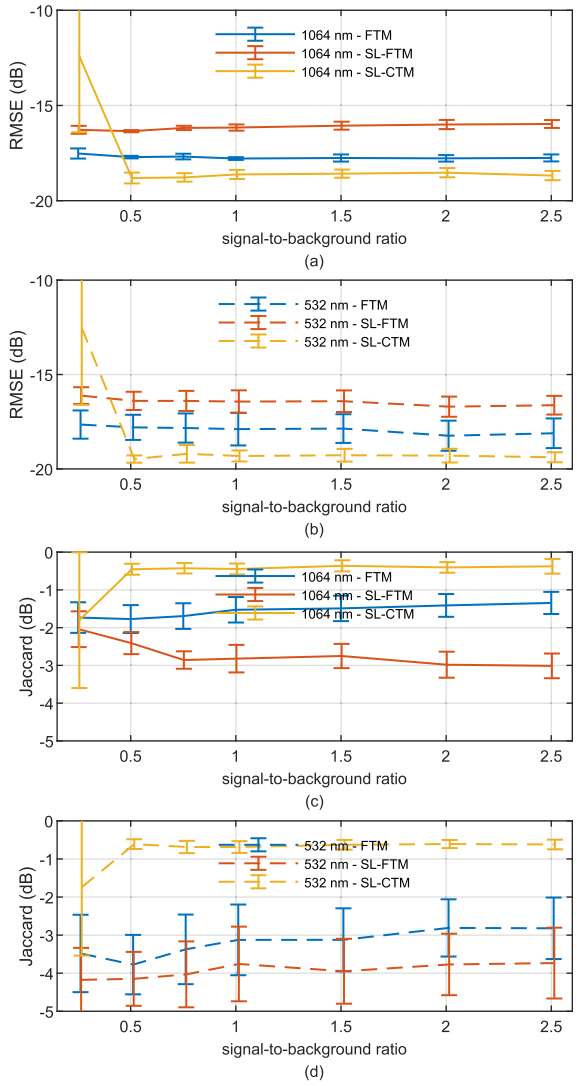

Fig. 6. Accuracy with 30-dB SBNR and varying SBR. (a) 1064-nm RMSE. (b) 532-nm RMSE. (c) 1064-nm Jaccard index. (d) 532-nm Jaccard index.

These combined effects result in low Jaccard measures (less than -3 dB or 0.5).

2) Varying Signal Plus Background to Noise With Constant SNR: In the second simulation, we fix SBNR at 30 dB (virtually zero additive noise) and adjust SBR to range from 0.25 to 2.5. The RMSE and Jaccard indices shown in Fig. 6 have similar trends as the additive noise case. FTM and SL-CTM have comparable accuracy and are 1–2 dB better than SL-FTM, which is still 5 dB better than the standard line tolerance. However, the Jaccard measure shows how SL-CTM recovers the surface profile with better agreement to ϕ than FTM and SL-FTM. The line fitting and interpolation of SL-CTM result in a smooth phase surface resulting in a larger size of $\mathcal{B}$. As in the previous simulation, SL-FTM still underestimates the surface height resulting in a smaller set $\mathcal{A}$ and lower Jaccard index than FTM.

C. Discussion

The SL-CTM and SL-FTM offer distinct advantages. The contour tracing of CTM ensures the most accurate reconstruction of the phase profile and without the need for phase unwrapping. The interpolation from the traced lines to a surface establishes a smooth fit and better phase recovery than FTM. The incorporation of SL is very easy to implement and helps to automate the tracing process saving considerable preprocessing time. While these are clear advantages, it is noted that the line fitting step removes subtle fringe shift variation caused by the nonhomogeneous plasma. Also, the phase can only be recovered from within the image domain where the fringe lines are traced. Hence, the domain of the plasma must correspond to the region of the image that can be traced. In addition, the specific type of curve presented by the fringe lines must be designed if the mental model of step 3) of CTM is automated. The algorithm used in this work modeled the traced segments as either lines or Gaussian curves, and the mental model applied logic to recognize the segments that formed a single fringe line. However, if only a few interferograms are to be analyzed, the segments can be joined using a manual approach. The automated contour extraction aided by SL saves considerable time and does not require additional image processing to improve the clarity of the fringe lines.

The Fourier-based approach of FTM requires a different type and amount of preprocessing than CTM. First, the spatial frequency must be known or measured, and then, the spatial frequency filter must be designed to pass the spectral region representing the phase shift. These steps are usually iterative but can be automated. SL was used in the Monte Carlo to improve the automatic measurement of (κ_y, κ_z). Without SL or another form of prefiltering, FTM will require a manual calculation of the fringe lines. For cases where the same optical setup is used, this step may be unimportant. The advantages of FTM are as follows: 1) its ability to recover the phase for an arbitrary yz domain and 2) to capture effects of subtle fringe line variation. Thus, in some cases, the phase profile recovered by FTM may appear less smooth than those of CTM, as it naturally captures spatial perturbations of the fringe lines. However, FTM requires a robust phase unwrapping method and performs poorly when the spatial frequency is low with respect to the bandpass filter width. The Jaccard index showed how significant the dc leakage affected the resulting surface. For density measurements where the final step is to invert (2), the rippled line shift surface will limit the accuracy of the volumetric density measurement.

V. Conclusion

The SL algorithm has been presented as a prefiltering stage that enables automation of the FTM and the CTM, which measure 2-D relative phase from optical interferometry. The SL filtering was shown to greatly improve fringe line visibility of measured interferograms from plasma diagnostics. As part of the SL-FTM process, the spectral carrier frequency and bandwidth were measured without a priori knowledge, and without need of an iterative algorithm. The accuracies of FTM, SL-FTM, and SL-CTM were compared using a Monte Carlo simulation of over 500 noisy images with realistic background variation.

The error analysis showed how each algorithm had an error at least three times below the standard requirement

of 0.05 lines needed for plasma diagnostics. In addition, while CTM is accepted as the most accurate method, it is impractical to manually trace the lines of such a large number of images. Thus, the error analysis of SL-CTM provided a first insight into how CTM compares with FTM for a diverse set of images. Finally, an analysis with the Jaccard similarity measure explained how the resulting 2-D line-shift surface of SL-FTM was smoother than FTM's result, but also underestimated the maximum line shift resulting in the larger error of SL-FTM. SL-FTM and SL-CTM have been shown to enable bulk-automated processing of optical interferometry with open fringe lines, such as from side-on views of exploded-wire experiments.

REFERENCES

[1] G. S. Sarkisov, S. E. Rosenthal, K. R. Cochrane, K. W. Struve, C. Deeney, and D. H. McDaniel, "Nanosecond electrical explosion of thin aluminum wires in a vacuum: Experimental and computational investigations," *Phys. Rev. E, Stat. Phys. Plasmas Fluids Relat. Interdiscip. Top.*, vol. 71, no. 4, pp. 1–14, Apr. 2005.

[2] A. Hamilton, V. I. Sotnikov, and G. S. Sarkisov, "Vaporization energy and expansion velocity of electrically exploding aluminum and copper fine wires in vacuum," *J. Appl. Phys.*, vol. 124, no. 12, pp. 1–6, Sep. 2018, doi: 10.1063/1.5025831.

[3] M. A. Saville, "2D relative phase reconstruction in plasma diagnostics," in *Optical Interferometry*, M. Bhowmick, Ed. Rijeka: Rijeka, Croatia: InTechOpen, 2022, ch. 3, doi: 10.5772/intechopen.104748.

[4] M. Takeda, H. Ina, and S. Kobayashi, "Fourier-transform method of fringe-pattern analysis for computer-based topography and interferometry," *J. Opt. Soc. Amer.*, vol. 72, no. 1, p. 156, Jan. 1982.

[5] M. Takeda, "Temporal versus spatial carrier techniques for heterodyne interferometery," *Proc. SPIE*, vol. 813, pp. 329–330, Jan. 1987.

[6] M. Takeda, "Spatial-carrier fringe-pattern analysis and its applications to precision interferometry and profilometry: An overview," *Ind. Metrol.*, vol. 1, no. 2, pp. 79–99, Jun. 1990.

[7] J. H. Massig and J. Heppner, "Fringe-pattern analysis with high accuracy by use of the Fourier-transform method: Theory and experimental tests," *Appl. Opt.*, vol. 40, no. 13, p. 2081, May 2001.

[8] A. Zaraś-Szydłowska et al., "Implementation of amplitude–phase analysis of complex interferograms for measurement of spontaneous magnetic fields in laser generated plasma," *AIP Adv.*, vol. 10, no. 11, pp. 1–20, Nov. 2020.

[9] G. F. Swadling, "An experimental investigation of the azimuthal structures formed during the ablation phase of wire array Z-pinches," Ph.D. dissertation, Dept. Phys., Imperial College, London, U.K., 2012.

[10] J. Wu et al., "Atomization and merging of two Al and W wires driven by a 1 kA, 10 ns current pulse," *Phys. Plasmas*, vol. 23, no. 11, pp. 1–9, Nov. 2016.

[11] A. Hamilton, M. A. Saville, and V. Sotnikov, "Dual-wavelength interferometric measurement of electrically exploded aluminum and copper wires in low-pressure air for electron and ion density calculation," *IEEE Trans. Plasma Sci.*, vol. 48, no. 9, pp. 3144–3151, Sep. 2020.

[12] S. Nakayama, H. Toba, N. Fujiwara, T. Gemma, and M. Takeda, "Enhanced Fourier-transform method for high-density fringe analysis by iterative spectrum narrowing," *Appl. Opt.*, vol. 59, no. 29, p. 9159, Oct. 2020.

[13] M. A. Saville, "2D relative phase reconstruction of low-contrast plasma interferometry," in *Proc. IEEE Res. Appl. Photon. Defense Conf. (RAPID)*, Miramar, FL, USA, Sep. 2022, pp. 1–2.

[14] G. S. Sarkisov, I. L. Beigman, V. P. Shevelko, and K. W. Struve, "Interferometric measurements of dynamic polarizabilities for metal atoms using electrically exploding wires in vacuum," *Phys. Rev. A, Gen. Phys.*, vol. 73, no. 4, pp. 1–8, Apr. 2006.

[15] J. M. Huntley, "Automated fringe pattern analysis in experimental mechanics: A review," *J. Strain Anal. Eng. Des.*, vol. 33, no. 2, pp. 105–125, Feb. 1998.

[16] J. M. Bioucas-Dias and G. Valadao, "Phase unwrapping via graph cuts," *IEEE Trans. Image Process.*, vol. 16, no. 3, pp. 698–709, Mar. 2007.

[17] J. M. Maciel, F. J. C. Rodríguez, M. M. González, F. G. P. Lecona, and V. M. D. Ramírez, "Digital processing techniques for fringe analysis," in *Optical Interferometry*, A. A. Banishev, M. Bhowmick, and J. Wang, Eds. Rijeka, Croatia: InTechOpen, 2017, ch. 1, doi: 10.5772/66474.

[18] M. Takeda and H. Yamamoto, "Fourier-transform speckle profilometry: Three-dimensional shape measurements of diffuse objects with large height steps and/or spatially isolated surfaces," *Appl. Opt.*, vol. 33, no. 34, p. 7829, Dec. 1994.

Michael A. Saville (Senior Member, IEEE) received the B.S. degree in electrical engineering from Texas A&M University, College Station, TX, USA, in 1997, the M.S. degree in electrical engineering from the U.S. Air Force Institute of Technology (AFIT), Wright-Patterson Air Force Base, OH, USA, in 2000, and the Ph.D. degree in electrical and computer engineering from the University of Illinois Urbana-Champaign, Champaign, IL, USA, in 2006.

He was previously on faculty at Wright State University, Dayton, OH, USA, where this work was performed. He is currently a Professor of electrical engineering at AFIT. He is also a registered professional engineer in OH, USA. His research interests include the applications of electromagnetics and signal processing with an emphasis on radar imaging and target recognition.

Dr. Saville is Life Member of the Society of Hispanic Professional Engineers and serves as an Associate Editor for *Progress in Electromagnetics Research Journal* and *IET Electronics Letters*.

Andrew J. Hamilton (Senior Member, IEEE) received the B.S. degree in engineering physics and the M.S. degree in electrical engineering from Wright State University, Dayton, OH, USA, in 2014 and 2017, respectively.

He is currently an Electronics Engineer with the Materials and Manufacturing Directorate, U.S. Air Force Research Laboratory, Wright-Patterson Air Force Base, OH, USA. His technical expertise focuses on electromagnetics and diagnostics of plasma properties. In studying ionospheric and electromagnetic interactions, he has led numerous field experiments that leveraged key research sites, such as the High-Frequency Active Auroral Research Program (HAARP), Alaska, and the now-defunct Arecibo Observatory, Puerto Rico. He leads the Low-Cost Space and In-Space Assembly and Manufacturing Programs for Air Force ManTech where he sponsors emerging and novel space technologies and supports their manufacturing maturation, ensuring significant return on investment for the defense industrial base.

James E. Caplinger , photograph and biography not available at the time of publication.